iScience

CellPress
OPEN ACCESS

Article

Angular dependent terahertz emission from the interplay between nanocrystal diamond film and plasmonic metasurface

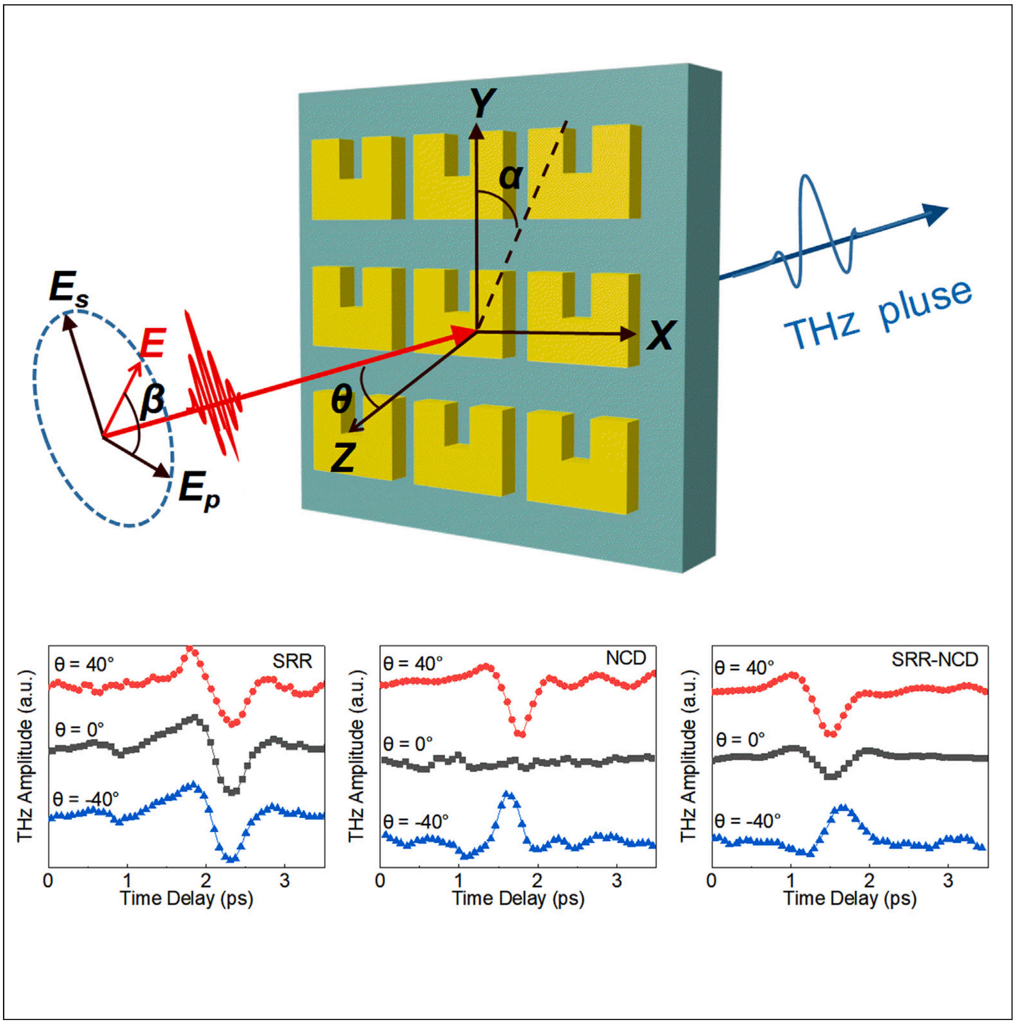

Shuangquan Fang, Wenpeng Guo, Yuanyuan Huang, ..., Jian Yi, Nan Jiang, Changzhi Gu

sqfang@yzu.edu.cn (S.F.)
yyhuang@nwu.edu.cn (Y.H.)
quanbaogang@iphy.ac.cn (B.Q.)
xlxuphy@nwu.edu.cn (X.X.)

Highlights

A split-ring resonator (SRR)-type metasurface was fabricated on a free-standing nanocrystal diamond (NCD) film

THz radiation can be generated by femtosecond pulses pumping the SRR-NCD metasurface

The mechanism of angular dependent THz emission is revealed

Fang et al., iScience *27*, 108939
February 16, 2024
https://doi.org/10.1016/j.isci.2024.108939

iScience

CellPress
OPEN ACCESS

Article

Angular dependent terahertz emission from the interplay between nanocrystal diamond film and plasmonic metasurface

Shuangquan Fang,[1,7,*] Wenpeng Guo,[1,2] Yuanyuan Huang,[3,*] Mingjian Shi,[3] Xuezeng Tian,[2] Baogang Quan,[2,5,6,*] Xinlong Xu,[3,*] Jian Yi,[4] Nan Jiang,[4] and Changzhi Gu[2]

SUMMARY

Composite structures integrated with metasurfaces and nonlinear films have emerged as alternative candidates to enhance nonlinear response. The cooperative interaction between the two components is complicated. Herein, a split-ring resonator (SRR)-type metasurface was fabricated on a free-standing nanocrystal diamond (NCD) film utilizing electron beam lithography, electron beam evaporation, and a lift-off process. The terahertz (THz) radiation from the SRR-NCD under normal incidence originates from the high-order magnetic resonance of SRR because the NCD film cannot produce detectable THz radiation at this incident angle. As increasing the incident angle, the contribution of the THz radiation from the NCD film gradually increases until reaching 40° incident angle limitation. The results indicate that this angular-dependent THz radiation is induced by the interplay between the NCD film and SRR. This study offers a new approach to investigate nonlinear processes in composite structures.

INTRODUCTION

In recent decades, due to the growth of photonics technology and semiconductor crystal growth technology, increasing types of materials produce terahertz (THz) emission under femtosecond optical pulse excitation, such as graphene,[1,2] transition metal dichalcogenides,[3,4] and Te nanotube.[5] Recent progress in plasmonic metasurfaces has allowed for efficient THz generation.[6–8] The split-ring resonator (SRR)-type metasurface is one of commonly used plasmonic metasurfaces. The nonlinear photocurrent induced by the symmetry breaking of the SRR allows it to produce strong THz radiation at normal incidence.[9–11] Meanwhile, metasurfaces can be easily integrated with other nonlinear materials or films using nano-manufacturing techniques. Integrating metasurfaces with other nonlinear materials, such as multi-quantum-well structures[12,13] or epsilon-near-zero films,[14] have emerged as alternative candidates to enhance nonlinear response. These integrated devices work at room temperature, can produce broadband THz radiation under femtosecond laser irradiation, which is expected to be a broadband THz source that can be used for bio-detection. In addition, this type of device allows to obtain control over the characteristics of the emitted THz radiation and can be integrated in compact systems. Nanocrystal diamond (NCD) film is an emerging functional carbon nanomaterial, experiencing excellent properties of diamond and unique properties of nanomaterials, such as a small size effect, surface effect, and quantum effect. These effects allow NCD films to acquire new electronic and optical properties that are unavailable in bulk diamond.[15,16] In addition, NCD can achieve enhanced nonlinear optical effects because of the small grain size and presence of surfaces, making it useful in potential applications, such as optical switching and wavelength conversion.[17] Several reports have been published on the nonlinear optical properties of NCD films, such as second- and third-harmonic generation.[17–19] Moreover, the high carrier mobility and high damage threshold of NCD films have led to investigation of the THz emission of NCD films. Recently, Xue et al. successfully detected THz emission from micro/nano-crystal diamond film under femtosecond optical pulses excitation.[20] As an emerging thin film material, NCD films can be combined with SRR, and the THz generation process from this composite structure attracts our attention.

Studying the THz generation mechanism is critical. THz radiation can be induced by linear or nonlinear processes on materials under femtosecond pulse excitation, such as diffusion and drift carrier,[21] photo-Dember effect,[22] optical rectification,[23] and photon drag effect.[24] The dominant process varies with the material and pump conditions. In many scenarios, several physical processes occur simultaneously in semiconductors under femtosecond pulse excitation, such as the competition between surface optical rectification and surface photocurrent

[1]College of Mechanical Engineering, Yangzhou University, Yangzhou 225127, China
[2]Beijing National Laboratory for Condensed Matter Physics, Institute of Physics, Chinese Academy of Sciences, Beijing 100190, China
[3]Shaanxi Joint Lab of Graphene, State Key Laboratory of Photon-Technology in Western China Energy, International Collaborative Center on Photoelectric Technology and Nano Functional Materials, Institute of Photonics & Photon-Technology, Northwest University, Xi'an 710069, China
[4]Ningbo Institute of Materials Technology and Engineering, Chinese Academy of Sciences, Ningbo 315201, China
[5]Songshan Lake Material Laboratory, Guangdong 523808, China
[6]University of Chinese Academy of Sciences, Beijing 100049, China
[7]Lead contact
*Correspondence: sqfang@yzu.edu.cn (S.F.), yyhuang@nwu.edu.cn (Y.H.), quanbaogang@iphy.ac.cn (B.Q.), xlxuphy@nwu.edu.cn (X.X.)
https://doi.org/10.1016/j.isci.2024.108939

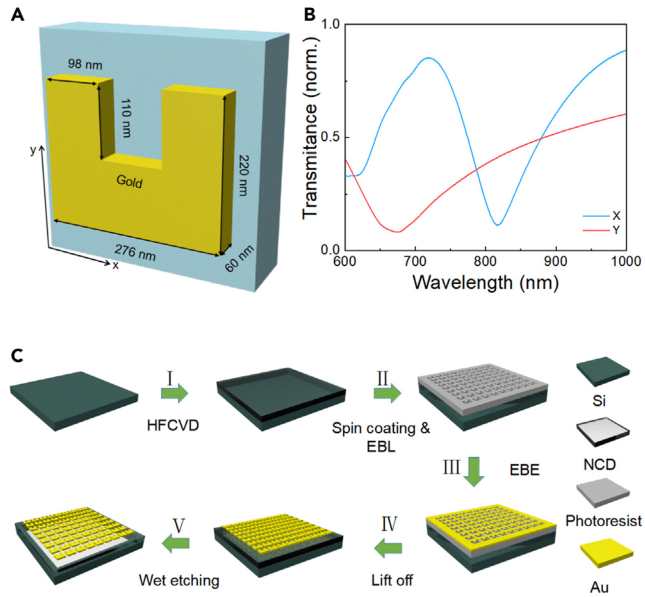

Figure 1. Design and fabrication of the SRR-NCD

(A) Typical SRR dimensions.

(B) Simulated transmission spectra of the SRR for horizontal (blue) and vertical polarizations (red) (relative to the SRR orientation in A).

(C) Schematic illustration of the fabrication flowchart of the SRR-NCD.

in MoS_2[3] as well as the interplay between the photon drag effect and photogalvanic effect in tellurium nanotubes.[5] Compared to single materials, the THz generation process in composite structures is complicated because the generation effects of the constituent materials are often coupled with each other. The interplay between different nonlinear effects in composite structures has been less reported.[25] These issues limit the development of composite THz emitting devices. In addition, the THz emission dependence on the incident angle varies for different materials. For instance, the THz emission from GaAs is proportional to the incident angle and reverses in polarity after changing the incident angle into opposite direction,[3] while the THz amplitude from SnS_2 decreases from -40° to 40° without polarity reversal.[4] The difference in THz dependence on the incident angle reflects the difference in the THz generation mechanism. Angular-resolved THz emission spectra obtained by accepting spectroscopic information emitted in different directions can further assist in the analysis of nonlinear processes in materials.

Herein, we have investigated the THz emission properties of a metasurface composed of an SRR array and free-standing NCD film (SRR-NCD). The angular dependence of THz emission from SRR-NCDs was investigated under a femtosecond laser excitation. The THz emission of the SRR-NCD exhibits 2-fold rotational symmetry with the polarization angle and 3-fold rotational symmetry with regard to the azimuthal angle at incident angles of 0° and 40°. Combined with the THz radiation dependences on the pump fluence and incident angle, we have confirmed that the THz radiation from the SRR-NCD originates from the cooperative interaction of the SRR and NCD film under oblique incidence. Additionally, by investigating the THz radiation dependence on the incident angle for the SRR, NCD, and SRR-NCD films, the THz radiation contribution ratio between the SRR and NCD films can be calculated. The contribution ratio of the NCD film to the SRR for THz emission is 2.5:1 at 40° incidence. This study lays a foundation for the potential applications of SRR-NCDs in functional THz emission devices.

Experiments and methods

Metasurface design and fabrication

The SRR has multiple resonance modes which can be excited at different wavelengths.[26,27] In this experiment, the output amplified laser pulse of the THz emission spectroscopy setup is a central wavelength of 800 nm. The metasurface shape should be designed to induce magnetic mode resonance under femtosecond (fs) pulse excitation.[9] As such, the obvious selection would be SRRs for THz generation in most of the reported works. The core structural parameters are lattice constants and SRR lengths. On the one hand, as increasing the lattice constant, the resonant strength decreases to some extent due to reduced interaction between the SRRs, while the resonant frequency remains unchanged.[28] On the other hand, the SRRs are equivalent to a typical inductor-capacitor (LC) resonant circuit of resonant frequency $f = 1/2\pi(LC)^{1/2}$, where L and C are the equivalent inductance and the equivalent capacitance of the SRR gap.[28] Thus, the resonant frequency is inversely proportional to the unit cell sizes, which should be matched to the excitation wavelength to induce electromagnetic resonance. Therefore, the dimensions of the SRR were determined by CST Studio Suite 2016 with parametric scanning, making its high-order resonant mode can be excited at 800 nm. Figure 1A shows the dimension schematic of the designed SRR. The simulated linear transmission through the SRR (Figure 1B) presents a resonant dip at 800 nm for polarization parallel to the base of the SRR.

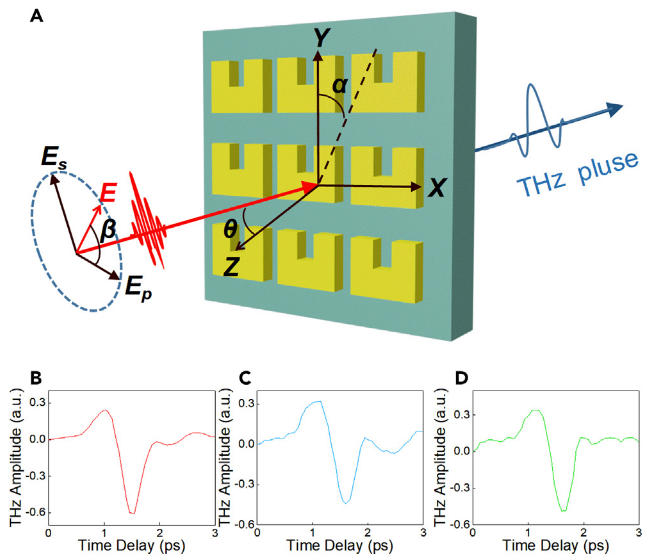

Figure 2. Simplified diagram of angle-resolved THz measurement

(A) Diagram of experimental setup for the THz generation. The angles θ, α, and β represent the incident angle, azimuthal angle, and polarization angle, respectively.

(B–D) Typical THz time-domain signals measured with varied incident angle, azimuthal angle, and polarization angle, respectively.

The detailed fabrication process of the SRR-NCD is shown in Figure 1C. A p-type (100) silicon wafer was cleaned with acetone, ethyl alcohol, and deionized water (DW) using an ultrasonic cleaner, and then dried on a hot plate. Thereafter, an NCD film with 4 μm-thickness was deposited on the silicon substrate surface utilizing a hot filament chemical vapor deposition system (HFCVD) (Step I). Figure S1 shows the Raman spectroscopy and ellipsometric characterization of the NCD film. The SRR-type metasurface on the NCD film was fabricated using electron-beam lithography (EBL) and electron-beam evaporation (EBE), followed by a lift-off procedure. The silicon wafer with the NCD film was spin-coated with polymethyl methacrylate (PMMA) and ethyl lactate (EL) bilayer electron-beam resist, and then exposed in an EBL system (JEOL, 6300FS) (Step II). The exposed wafer was developed using a MIBK/IPA developer to obtain the SRR array pattern. Subsequently, a metallic film of 5 nm Ti and 60 nm Au was deposited by an EBE system (Step III). After deposition, a lift-off process was performed to obtain the SRR structure (Step IV). Finally, in order to eliminate the influence of the silicon substrate on the measurement, the silicon substrate was removed by a nitric acid/hydrofluoric acid mixture using paraffin as a mask (Step V). SEM images of the SRR-NCD are shown in Figure S2 in supplemental information.

Experimental setup of the terahertz emission spectroscopy

A THz emission spectroscopy system (Figure S3) was used to measure the THz emission characteristics of the SRR-NCD. Figure 2 shows a simplified diagram of the THz radiation generated by the SRR-NCD under an 800 nm fs pulse excitation, where XYZ is the laboratory coordinate system. The incident angle is labeled as θ, which is between the incident wave vector and the normal of the sample, and can be changed by spinning the sample in the XZ plane. The sample can be rotated in the XY plane to alter the azimuthal angle α. The polarization angle β was controlled using a half-wave plate (HWP). Figures 2B–2D are typical THz time-domain signals measured with varied incident angle, azimuthal angle, and polarization angle, respectively.

RESULTS AND DISCUSSION

THz emission from the SRR-NCD under 0° and 40° incidences

The THz emission measurement of the SRR-NCD was performed with an 800 nm fs pulse at a fixed pump fluence of 0.48 mJ/cm^2. Figures 3A and 3B show the time-domain signals of the THz emission excited by the p- (P_{in}) and s-polarized (S_{in}) pump beams under 0° and 40° incidence, respectively. With the limitation by our experimental configuration, although the THz emission signal will further increase as the increasing of incident angle, we currently focus on the results of 40° incidence. According to Figure 3A, the observable THz emission is generated under P_{in} excitation with a normal incident angle, while no THz radiation is detected under S_{in} excitation. However, THz emission can be excited by both P_{in} and S_{in} excitations under 40° incidence (Figure 3B). At normal incidence, the spectral bandwidth of the THz radiation excited by p-polarization is ~2 THz, whereas no significant THz radiation can be observed under s-polarization excitation (Figure 3C). For THz emission under 40° incidence, the spectral bandwidth is typically equal (~2 THz) under P_{in} and S_{in} excitations; however, the intensity of the THz radiation produced under P_{in} illumination is larger than that under S_{in} illumination, and the THz waveform polarities are reversed under P_{in} and S_{in} excitations. Therefore, the THz radiation under both 0° and 40° incidences is dependent on the polarization condition of the pump beam. This comes after one of the key characteristics of second-order nonlinear optical effects, such as photon drag effect or photogalvanic effect.[2,29]

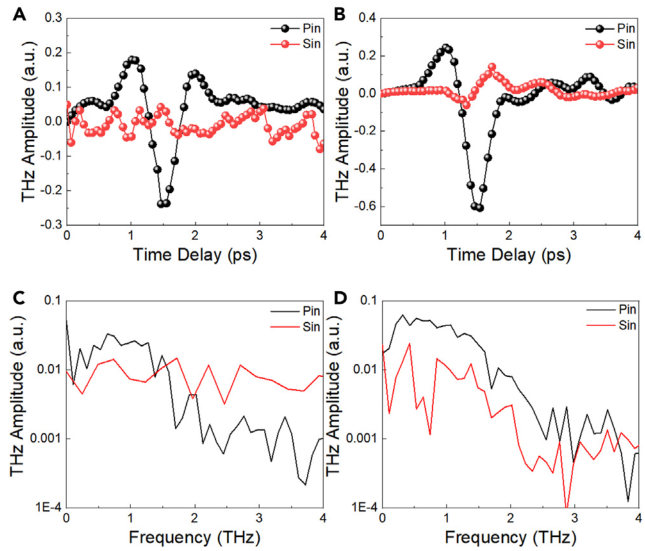

Figure 3. THz radiation properties from the SRR-NCD under 0° and 40° incidences

(A and B) The time-domain THz pulses from the SRR-NCD excited by p- (P_{in}, black) and s-polarized (S_{in}, red) pump beam under (A) 0° and (B) 40° incidences.
(C and D) The corresponding spectral amplitudes generated from the SRR-NCD under (C) 0° and (D) 40° incidences.

We can tentatively deduce that the THz radiation mechanism of the SRR-NCD is relevant to the nonlinear optical effect. However, the SRR-NCD exhibits a significant difference in THz radiation at 0° and 40° incidence. This perhaps connected to different nonlinear optical effects. Meanwhile, according to the current measurement from Lock-in amplifier, the absolute value THz electric field of the SRR-NCD has been obtained as 102 V/m, which is larger than the absolute THz electric field of the MoS_2 crystal of 96.72 V/m[30] and WSe_2 of 23.15 V/m.[31] The peak power of the THz radiation is estimated as $P_{THz(SRR\text{-}NCD)}$ = 10.8 μW (see the detailed calculation in supplemental information).

Since the pump fluence dependence of the THz amplitude can distinguish the linear and nonlinear processes in materials,[5] we have investigated the THz radiation of the SRR-NCD in relation to the pump fluence under 0° and 40° incidence. With the pump fluence increasing from 0.19 mJ/cm^2 to 0.76 mJ/cm^2, the THz amplitude of the SRR-NCD increases linearly with the pump fluence under 0° and 40° incidences, as shown in Figure 4A. We can confirm that the THz radiation from the SRR-NCD is dominated by the second-order nonlinear optical effects, because the amplitude of the THz radiation is quadratic with the pump electric field by employing $E_{THz} \propto E(\omega) \cdot E(\omega) \cdot \chi^{(2)} \propto I_{pump}$.[30]

Polarization dependence of THz generation under 0° and 40° incidences

To further identify the relationship between the THz emission of the SRR-NCD and pump beam polarization states, we have measured the THz amplitude of the SRR-NCD varying with the polarization angle (β in Figure 2A) under 0° (Figure 4C) and 40° (Figure 4F) incidences. For direct comparison, the polarization angle dependence of THz amplitude was also recorded for the bare NCD film (Figure 4D) and SRR at 0° (Figure 4B) and 40° (Figure 4E) incidences. The polarization angle is varied from 0° to 360° (0°, 180°, and 360° correspond to P_{in} excitation, while 90° and 270° correspond to S_{in} excitation). As shown in Figure 4C, the THz emission of the SRR-NCD at normal incidence exhibits 2-fold rotational symmetry with varying β in the whole range. The maximum value of the THz radiation presents at P_{in} excitation, and the upper bound (close to zero) occurs at S_{in} excitation. Such dependence is consistent with the SRR, as shown in Figure 4B. When the SRR is illuminated under S_{in} excitation, only the electric dipole resonance can be excited. In this mode, the nonlinear currents are out of phase, hence interfering destructively.[9] As a result, there isn't any THz emission visible in the far field. As shown in Figure 4F, the THz radiation of the SRR-NCD also demonstrates 2-fold rotational symmetry at 40° incidence. However, the THz emission under the S_{in} excitation is not zero and transfers toward the positive direction (as noted by the red arrow in Figure 4F). This is because the symmetry of the SRR's electric dipole resonance mode is broken under the oblique incidence, which enables the detection of THz radiation (Figure 4E). Additionally, the NCD film does not contribute to the amplitude shift because the THz radiation of the NCD film under P_{in} and S_{in} excitation is different in amplitude but same in polarity (both present negative values in Figure 4D). Moreover, the THz emission of the SRR-NCD excited by the P_{in} pump beam enhances and significantly transfers toward the negative direction (as noted by the blue arrow in Figure 4F) under 40° incidence. At an incident angle of 40°, the NCD film exhibit strong THz radiation under P_{in} excitation. Thus, the shift was owing to the NCD film. According to the aforementioned findings, the SRR metasurface primarily contributes to the THz generation of the SRR-NCD metasurface under normal incidence, whereas the THz generation under oblique incidence originates from the cooperative contact between the SRR metasurface and NCD film.

Azimuthal angle dependence of THz generation under under 0° and 40° incidences

On account of the previous analysis, the THz emission from the SRR-NCD can be considered as the cooperative interaction of the nonlinear current in the SRR and NCD. The nonlinear current in the SRR is induced by the ponderomotive acceleration of photoelectrons (see the THz radiation

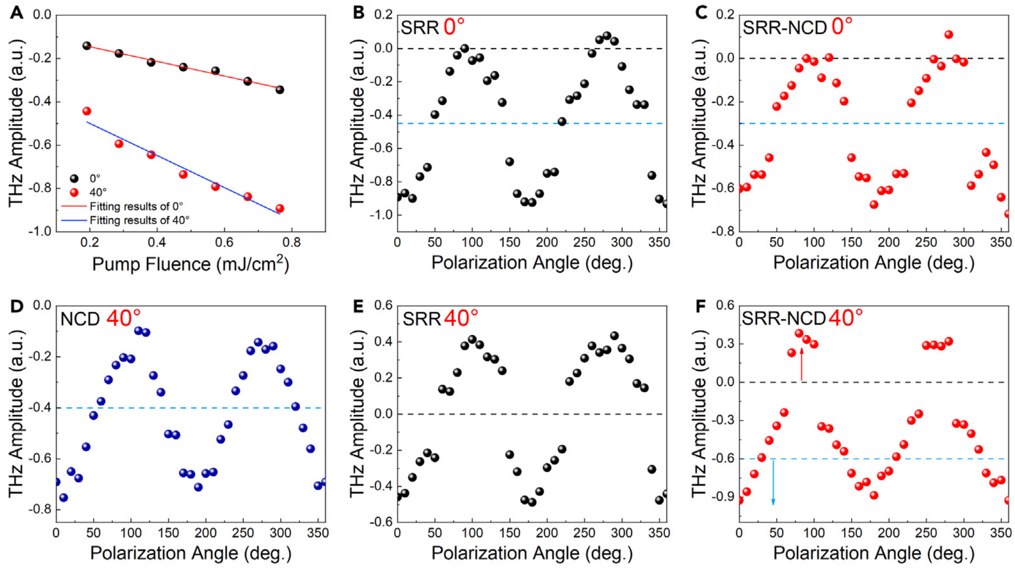

Figure 4. Pump fluence and polarization angle dependence of THz radiation

(A) Dependence of THz amplitude of the SRR-NCD metasurafce on pump fluence under 0° (black) and 40° (red) incidences. The experimental and fitting results are depicted with dot and solid lines, respectively.

(B–F) The polarization angle dependences of the THz peak-to-valley values of (B) SRR and (C) SRR-NCD under 0° incidence and (D) NCD, (E) SRR, and (F) SRR-NCD under 40°incidence.

mechanism of the SRR metasurface in the supplemental information). This nonlinearity changes with the rotation azimuthal angle because it flows along the structure. Thus, the THz radiation from the SRR can be influenced by the azimuthal angle (Figure S5B). However, the nonlinear current in the NCD film is induced by the photon drag effect.[20] Because NCD is a polycrystalline material, the anisotropy of grain orientation enables THz amplitude to be independent of the azimuthal angle (Figure S4). Therefore, the THz generation mechanism from the SRR-NCD under different incidences can be further confirmed from the THz emission dependence on the azimuthal angle. The azimuthal angle dependence of THz radiation under 0° and 40° incidences are measured at a fixed pump fluence of 0.48 mJ/cm^2 (Figure 5). According to Figure 5A, as the azimuthal angle varied from 0° to 360° under the normal incidence, the THz radiation generated from the SRR-NCD exhibits 3-fold rotational symmetry. This is in line with the results of the SRR, which is represented in Figure S5B. Therefore, at normal incidence, the THz emission from the SRR-NCD originates from the SRR. At 40° incidence, the THz emission from the SRR-NCD also exhibits 3-fold rotational symmetry as the azimuthal angle α changed from 0° to 360°. However, the THz radiation from the SRR-NCD under 40° incidence remained almost negative over the entire angle range. This is different from the SRR, in which the polarity of the THz radiation can reverse with the change in azimuthal angle. Moreover, the THz emission amplitude from the SRR-NCD under 40° incidence transfers toward the negative direction (as noted by the black arrowhead in Figure 5B). This is attributed to the contribution of the azimuth-independent photon drag current in the NCD.

Simulation of the angular dependent THz generation

According to the different THz radiation characteristics of the SRR-NCD at different incident angles, we can extract the different contributions of SRR and NCD to the THz generation at different incident angles, which is consistent with simulation results. The simulations were based on

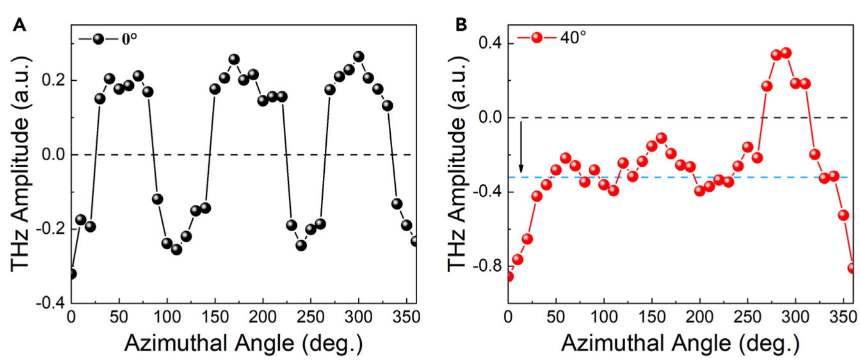

Figure 5. Azimuthal angle dependence of THz generation from the SRR-NCD under different incident angles

(A) 0° and (B) 40° incidences.

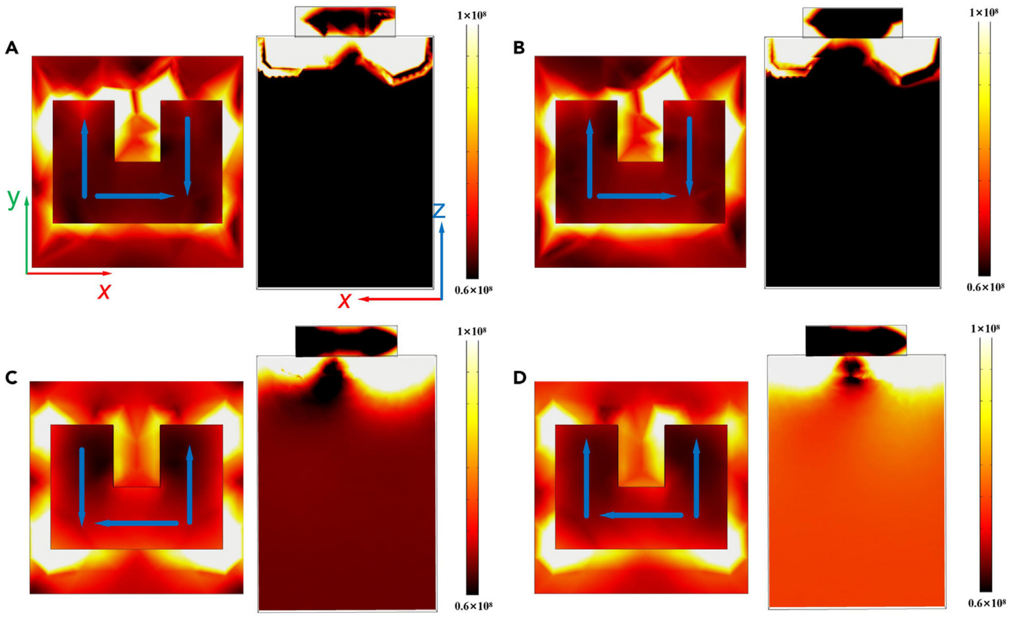

Figure 6. Electric field distributions of SRR-NCD and SRR metasurfaces

Simulated Ez (left panels) and Ey (right panels) components of electric field distributions of the SRRs at (A) normal incidence and (B) 40° incidence, respectively. Simulated Ez (left panels) and Ey (right panels) components of electric field distributions of the SRR-NCD at (C) normal incidence and (D) 40° incidence, respectively. The flowing directions of surface currents are labeled by the blue arrows.

COMSOL Multiphysics. In this model, both gold and NCD are considered as plasmonic materials that can be quantitatively described by a Drude model, $\varepsilon_{NCD}(\omega) = \varepsilon'(\omega) - i\varepsilon''(\omega) = \varepsilon_\infty - \omega 2\ p/(\omega^2 + i\omega\gamma)$, where ε_∞ is the infinite frequency permittivity, $\omega_p = \sqrt{ne^2/(\varepsilon_0 m)}$ is the plasma frequency determined by the carrier density n, and γ is the collision frequency. For gold, these parameters were set as $\varepsilon_\infty = 1$, $\omega_p = 1.366 \times 10^{16}$ rad s^{-1}, and $\gamma = 1.2 \times 10^{14}$ rad s^{-1}.[14] For the NCD, these parameters were set as $\varepsilon_\infty = 5.6$, $\omega_p = 2.1981 \times 10^{13}$ rad s^{-1}, and $\gamma = 5.117 \times 10^{11}$ rad s^{-1}.

The THz radiation of the SRR and SRR-NCD metasurfaces are related to the strength of the electric field distributions. As show in Figures 6A and 6B, the electric field Ey component intensity of SRRs at 0° incidence is stronger than that at 40° incidence, which is consistent to the experimental result as the radiated THz amplitude of SRRs at 0° incidence is larger than that at 40° incidence. On the contrary, the Ey electric field intensity of the SRR-NCD metasurface at 0° incidence is obviously lower than that at 40° incidence (Figures 6C and 6D), corresponding to the lower THz amplitude at 0° incidence compared with that at 40° incidence. Due to the interplay between the SRR and NCD film, the electric field distributions of the SRR-NCD at 40° incidence is much larger than that at normal incidence. The simulation results match the experiments. The resonance mode corresponding to the previous electric field distribution diagram is given through the surface photocurrents distribution, as the Ez electric field distributions shown in Figure 6. The resonance modes of SRR and SRR-NCD both exhibit high-order magnetic resonance at different incident angles.[32]

Evolution of THz radiation contributions

To further analyze the angular-dependent properties of the SRR-NCD, we have measured the dependence of the peak-to-valley values of the THz emission as a function of the incident angle for the NCD film, SRR, and SRR-NCD (Figure 7A) at a fixed pump fluence of 0.48 mJ/cm^2. The pump beam polarization state was set to p-polarization throughout the duration of the measurement. The THz emission of the NCD film is proportional to the incident angle in either the positive or negative direction. The negative value indicates that the THz waveform reverses after changing the incident angle into opposite direction. These reversed polarities indicate the opposite direction of the nonlinear current. Notably, the THz emission amplitude of the NCD film under normal incidence is zero, which is in line with the characteristics of the photon drag effect.[2] However, the THz amplitude of the SRR is the largest under normal incidence, then decreases in amplitude as increasing the incident angle. Meanwhile, the THz radiation from the SRR demonstrates no polarity change with an incident angle from −40° to 40°. Therefore, the direction of the nonlinear current induced by the ponderomotive acceleration of photoelectrons in the SRR is independent of the incident direction. Compared to NCD, the apparent THz radiation at normal incidence can be observed in SRR-NCD, which suggests the significant contribution of SRR. Moreover, the THz amplitude of the SRR-NCD film significantly transfers toward the negative direction (as noted by the blue arrow in Figure 7A) relative to the NCD film. Thus, the THz generation mechanism from the SRR-NCD under oblique incidence is complex.

Based on the previous analysis, SRR-NCD produces angular-dependent THz emission owing to the interplay between the NCD film and SRR. THz time-domain emission waveforms of the SRR, NCD, and SRR-NCD at three typical incident angles (0°, −40°, and 40°) are shown in

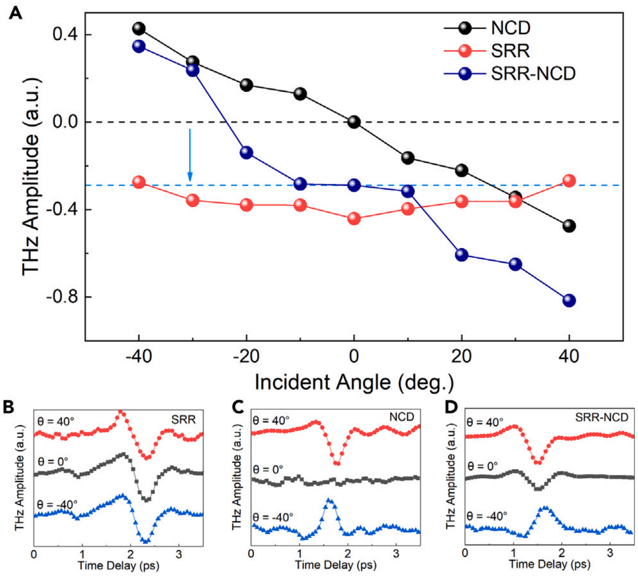

Figure 7. THz radiation dependence on the incident angle

(A) THz peak-to-valley values as a function of incident angle of NCD (black), SRR (red) and SRR-NCD (blue), respectively.

(B–D) THz time-domain signals of (B) SRR, (C) NCD, and (D) SRR-NCD under 0°, −40°, and 40° incidences, respectively.

Figures 6C, 6D, and 7B, respectively. As shown in Figure 7B, the amplitude of the THz pulse is nearly equal from −40° to 40° incidences in the SRR without polarity reversal. In terms of the NCD film (Figure 7C), the THz amplitude is almost zero under normal incidence since the photon drag current vanishes at symmetric non-equilibrium distribution of carriers along the positive and negative directions.[33] Meanwhile, the measured THz waveforms at −40° and 40° have the same amplitude and opposite polarity. The apparent THz signal is observed at 0° incidence in the SRR-NCD, as shown in Figure 7D. Because only the SRR can generate THz emission under normal incidence, the THz emission of the SRR-NCD is nearly 100% from the contribution of the SRR component under 0° incidence. Meanwhile, the measured THz waveforms at −40° and 40° incidence have opposite signs. Note that the THz emission at 40° is larger than that at −40° incidence, which is ascribed to the concurrent contribution of the SRR and NCD. Because the nonlinear current in the SRR is independent of the incident direction, the photocurrent components generated from the SRR and NCD are synchronous and play a constructive role in the THz radiation in the positive incident direction. After reversing the incident direction, the nonlinear photocurrent from the NCD flows along the contrary direction compared to the nonlinear photocurrent from the SRR, causing an adverse effect on the THz radiation in the negative incident direction. Thus, we can calculate the THz contribution ratio of the NCD and SRR at oblique incidence, which is approximately 2.5:1 for the THz radiation from the SRR-NCD under 40° incidence (see the detailed calculation in the supplemental information).

Conclusion

We have fabricated an SRR-NCD metasurface using EBL, EBE, and lift-off processes. The angular-dependent THz emission from SRR-NCD was observed under femtosecond laser excitation. The THz radiation originates from the ponderomotive acceleration of photoelectrons in the SRR combined with the photon drag effect in the NCD. The THz emission of the SRR-NCD under normal incidence is solely from the SRR. While the contribution ratio between the NCD and SRR is approximately 2.5:1 for the THz radiation from the SRR-NCD under 40° incidence, on the basis of the incident angle dependence of THz radiation. This work provides an insight into the nonlinear processes in the SRR-NCD composite structure, which unveils the interplay between the ponderomotive acceleration of photoelectrons and the photon drag effect.

Limitations of the study

In this study, we fabricated a split-ring resonator-type metasurface on a free-standing nanocrystal diamond film. However, the manufacture of the structure is still the main challenge due to the dense arrangement of SRRs and the adverse effects of the silicon etching process.

STAR★METHODS

Detailed methods are provided in the online version of this paper and include the following:

- KEY RESOURCES TABLE
- RESOURCE AVAILABILITY
  - Lead contact
  - Materials availability

- Data and code availability
- EXPERIMENTAL MODEL AND STUDY PARTICIPANT DETAILS
- METHOD DETAILS
- QUANTITATION AND STATISTICAL ANALYSIS
- ADDITIONAL RESOURCES

SUPPLEMENTAL INFORMATION

Supplemental information can be found online at https://doi.org/10.1016/j.isci.2024.108939.

ACKNOWLEDGMENTS

This work was supported by the National Natural Science Foundation of China under grant nos. 61888102, 11974386, 62174179, 12074420, U21A20140, 61905274, and 12261141662 and the Strategic Priority Research Program of the Chinese Academy of Sciences (CAS) under grant nos. XDB33000000 and XDB28000000. This work was also supported by the Youth Fund of the Chinese Academy of Sciences (No. JCPYJJ-22030).

AUTHOR CONTRIBUTIONS

X.X. conceived the idea and designed the metasurface. W.G., M.S., X.T., J.Y., and N.J. performed the experiment under the supervision of Y.H. and B.Q., S.F., W.G. wrote the article and assisted with the article revision by Y.H. and B.Q. The project is supervised by B.Q. and C.G.

DECLARATION OF INTERESTS

The authors declare no conflicts of interest.

Received: March 17, 2023
Revised: November 15, 2023
Accepted: January 15, 2024
Published: January 18, 2024

REFERENCES

1. Novoselov, K.S., Fal'ko, V.I., Colombo, L., Gellert, P.R., Schwab, M.G., and Kim, K. (2012). A roadmap for graphene. Nature *490*, 192–200. https://doi.org/10.1038/nature11458.
2. Bahk, Y.-M., Ramakrishnan, G., Choi, J., Song, H., Choi, G., Kim, Y.H., Ahn, K.J., Kim, D.-S., and Planken, P.C.M. (2014). Plasmon Enhanced Terahertz Emission from Single Layer Graphene. ACS Nano *8*, 9089–9096. https://doi.org/10.1021/nn5025237.
3. Huang, Y., Zhu, L., Yao, Z., Zhang, L., He, C., Zhao, Q., Bai, J., and Xu, X. (2018). Terahertz Surface Emission from Layered MoS_2 Crystal: Competition between Surface Optical Rectification and Surface Photocurrent Surge. J. Phys. Chem. C *122*, 481–488. https://doi.org/10.1021/acs.jpcc.7b09723.
4. Lei, Z., Huang, Y., Fan, Z., Du, W., He, C., Wang, H., Jin, Y., and Xu, X. (2020). Terahertz emission from in-plane and out-of-plane dipoles in layered SnS_2 crystal. Appl. Phys. Lett. *116*, 161901. https://doi.org/10.1063/5.0004701.
5. Cao, X., Huang, Y., Xi, Y., Lei, Z., Du, W., Han, T., Wang, J., Wang, H., Chang, J., Zhu, L., et al. (2022). Interplay between Ultrafast Shift Current and Ultrafast Photon Drag Current in Tellurium Nanotubes. ACS Photonics *9*, 3144–3155. https://doi.org/10.1021/acsphotonics.2c00993.
6. Polyushkin, D.K., Márton, I., Rácz, P., Dombi, P., Hendry, E., and Barnes, W.L. (2014). Mechanisms of THz generation from silver nanoparticle and nanohole arrays illuminated by 100 fs pulses of infrared light. Phys. Rev. B *89*, 125426. https://doi.org/10.1103/PhysRevB.89.125426.
7. Polyushkin, D.K., Hendry, E., Stone, E.K., and Barnes, W.L. (2011). THz Generation from Plasmonic Nanoparticle Arrays. Nano Lett. *11*, 4718–4724. https://doi.org/10.1021/nl202428g.
8. McDonnell, C., Deng, J., Sideris, S., Ellenbogen, T., and Li, G. (2021). Functional THz emitters based on Pancharatnam-Berry phase nonlinear metasurfaces. Nat. Commun. *12*, 30. https://doi.org/10.1038/s41467-020-20283-0.
9. Luo, L., Chatzakis, I., Wang, J., Niesler, F.B.P., Wegener, M., Koschny, T., and Soukoulis, C.M. (2014). Broadband terahertz generation from metamaterials. Nat. Commun. *5*, 3055. https://doi.org/10.1038/ncomms4055.
10. Tal, M., Keren-Zur, S., and Ellenbogen, T. (2020). Nonlinear Plasmonic Metasurface Terahertz Emitters for Compact Terahertz Spectroscopy Systems. ACS Photonics *7*, 3286–3290. https://doi.org/10.1021/acsphotonics.0c01012.
11. Keren-Zur, S., Tal, M., Fleischer, S., Mittleman, D.M., and Ellenbogen, T. (2019). Generation of spatiotemporally tailored terahertz wavepackets by nonlinear metasurfaces. Nat. Commun. *10*, 1778. https://doi.org/10.1038/s41467-019-09811-9.
12. Lee, J., Tymchenko, M., Argyropoulos, C., Chen, P.-Y., Lu, F., Demmerle, F., Boehm, G., Amann, M.-C., Alù, A., and Belkin, M.A. (2014). Giant nonlinear response from plasmonic metasurfaces coupled to intersubband transitions. Nature *511*, 65–69. https://doi.org/10.1038/nature13455.
13. Tymchenko, M., Gomez-Diaz, J.S., Lee, J., Belkin, M.A., and Alù, A. (2017). Highly-efficient THz generation using nonlinear plasmonic metasurfaces. J. Opt. *19*, 104001. https://doi.org/10.1088/2040-8986/aa82ca.
14. Lu, Y., Feng, X., Wang, Q., Zhang, X., Fang, M., Sha, W.E.I., Huang, Z., Xu, Q., Niu, L., Chen, X., et al. (2021). Integrated Terahertz Generator-Manipulators Using Epsilon-near-Zero-Hybrid Nonlinear Metasurfaces. Nano Lett. *21*, 7699–7707. https://doi.org/10.1021/acs.nanolett.1c02372.
15. Yoshikawa, M., Mori, Y., Obata, H., Maegawa, M., Katagiri, G., Ishida, H., and Ishitani, A. (1995). Raman scattering from nanometer-sized diamond. Appl. Phys. Lett. *67*, 694–696. https://doi.org/10.1063/1.115206.
16. Hainschwang, T., Notari, F., and Pamies, G. (2020). The origin of color of 1330 nm center diamonds. Diam. Relat. Mater. *110*, 108151. https://doi.org/10.1016/j.diamond.2020.108151.
17. Kozák, M., Trojánek, F., Rezek, B., Kromka, A., and Malý, P. (2012). Optical harmonic generation in nanocrystalline diamond. Phys. E Low-dimens. Syst. Nanostruct. *44*, 1300–1303. https://doi.org/10.1016/j.physe.2012.02.007.
18. Trojánek, F., Zídek, K., Dzurnák, B., Kozák, M., and Malý, P. (2010). Nonlinear optical properties of nanocrystalline diamond. Opt Express *18*, 1349–1357. https://doi.org/10.1364/OE.18.001349.
19. Preclíková, J., Kromka, A., Rezek, B., and Malý, P. (2010). Laser-induced refractive index changes in nanocrystalline diamond

membranes. Opt. Lett. *35*, 577–579. https://doi.org/10.1364/OL.35.000577.

20. Xue, X., Du, W., Tao, W., Huang, Y., Lei, Z., Zhu, L., Zou, Y., Liu, Y., Liu, G., Gu, C., et al. (2023). Giant photon-drag-induced ultrafast photocurrent in diamond for nonlinear photonics. Preprint at arXiv. https://doi.org/10.48550/arXiv.2309.11938.
21. Liu, K., Xu, J., Yuan, T., and Zhang, X.-C. (2006). Terahertz radiation from InAs induced by carrier diffusion and drift. Phys. Rev. B *73*, 155330. https://doi.org/10.1103/PhysRevB.73.155330.
22. Gu, P., Tani, M., Kono, S., Sakai, K., and Zhang, X.-C. (2002). Study of terahertz radiation from InAs and InSb. J. Appl. Phys. *91*, 5533–5537. https://doi.org/10.1063/1.1465507.
23. Rice, A., Jin, Y., Ma, X.F., Zhang, X.-C., Bliss, D., Larkin, J., and Alexander, M. (1994). Terahertz optical rectification from ⟨110⟩ zinc-blende crystals. Appl. Phys. Lett. *64*, 1324–1326. https://doi.org/10.1063/1.111922.
24. Obraztsov, P.A., Kanda, N., Konishi, K., Kuwata-Gonokami, M., Garnov, S.V., Obraztsov, A.N., and Svirko, Y.P. (2014). Photon-drag-induced terahertz emission from graphene. Phys. Rev. B *90*, 241416. https://doi.org/10.1103/PhysRevB.90.241416.
25. Saushin, A.S., Mikheev, G.M., Vanyukov, V.V., and Svirko, Y.P. (2021). The Surface Photogalvanic and Photon Drag Effects in Ag/Pd Metal-Semiconductor Nanocomposite. Nanomaterials *11*, 2827. https://doi.org/10.3390/nano11112827.
26. Seliuta, D., Šlekas, G., Vaitkūnas, A., Kancleris, Ž., and Valušis, G. (2017). Enhancement of higher-order plasmonic modes in a dense array of split-ring resonators. Opt Express *25*, 25113–25124. https://doi.org/10.1364/OE.25.025113.
27. Sheridan, A.K., Clark, A.W., Glidle, A., Cooper, J.M., and Cumming, D.R.S. (2007). Multiple plasmon resonances from gold nanostructures. Appl. Phys. Lett. *90*, 143105. https://doi.org/10.1063/1.2719161.
28. Linden, S., Enkrich, C., Wegener, M., Zhou, J., Koschny, T., and Soukoulis, C.M. (2004). Magnetic response of metamaterials at 100 terahertz. Science *306*, 1351–1353. https://doi.org/10.1126/science.1105371.
29. Obraztsov, P.A., Kaplas, T., Garnov, S.V., Kuwata-Gonokami, M., Obraztsov, A.N., and Svirko, Y.P. (2014). All-optical control of ultrafast photocurrents in unbiased graphene. Sci. Rep. *4*, 4007. https://doi.org/10.1038/srep04007.
30. Huang, Y., Zhu, L., Zhao, Q., Guo, Y., Ren, Z., Bai, J., and Xu, X. (2017). Surface Optical Rectification from Layered MoS_2 Crystal by THz Time-Domain Surface Emission Spectroscopy. ACS Appl. Mater. Interfaces *9*, 4956–4965. https://doi.org/10.1021/acsami.6b13961.
31. Chang, J., Wang, H., Lei, Z., Du, W., Huang, Y., Zhou, Y., Zhu, L., and Xu, X. (2021). Coherent Elliptically Polarized Terahertz Wave Generation in WSe_2 by Linearly Polarized Femtosecond Laser Excitation. J. Phys. Chem. Lett. *12*, 10068–10078. https://doi.org/10.1021/acs.jpclett.1c02770.
32. Enkrich, C., Wegener, M., Linden, S., Burger, S., Zschiedrich, L., Schmidt, F., Zhou, J.F., Koschny, T., and Soukoulis, C.M. (2005). Magnetic metamaterials at telecommunication and visible frequencies. Phys. Rev. Lett. *95*, 203901. https://doi.org/10.1103/PHYSREVLETT.95.203901.
33. Maysonnave, J., Huppert, S., Wang, F., Maero, S., Berger, C., de Heer, W., Norris, T.B., De Vaulchier, L.A., Dhillon, S., Tignon, J., et al. (2014). Terahertz Generation by Dynamical Photon Drag Effect in Graphene Excited by Femtosecond Optical Pulses. Nano Lett. *14*, 5797–5802. https://doi.org/10.1021/nl502684j.

STAR★METHODS

KEY RESOURCES TABLE

REAGENT or RESOURCE	SOURCE	IDENTIFIER
Software and algorithms		
COMSOL	COMSOL China Co., LTD	http://cn.comsol.com/

RESOURCE AVAILABILITY

Lead contact

Further information and requests for resources and reagents should be directed to and will be fulfilled by the lead contact, Shuangquan Fang (sqfang@yzu.edu.cn).

Materials availability

This study did not generate new unique reagents.

Data and code availability

(1) Data reported in this paper will be shared by the lead contact upon request.
(2) This paper does not report original codes.
(3) Any additional information required to reanalyze the data reported in this paper is available from the lead contact upon request.

EXPERIMENTAL MODEL AND STUDY PARTICIPANT DETAILS

The COMSOL software has been employed to analyze the electric field distributions of the metasurface.

METHOD DETAILS

The simulations were based on COMSOL Multiphysics. In this simulation, both gold and NCD are considered as plasmonic materials that can be quantitatively described by a Drude model, $\varepsilon(\omega) = \varepsilon'(\omega) - i\varepsilon''(\omega) = \varepsilon_\infty - \omega 2\,\mathrm{p}/(\omega^2 + i\omega\gamma)$, where ε_∞ is the infinite frequency permittivity, $\omega_\mathrm{p} = \sqrt{ne^2/(\varepsilon_0 m)}$ is the plasma frequency determined by the carrier density n, and γ is the collision frequency. For gold, these parameters were set as $\varepsilon_\infty = 1$, $\omega_\mathrm{p} = 1.366 \times 10^{16}$ rad s^{-1}, and $\gamma = 1.2 \times 10^{14}$ rad s^{-1}. For the NCD, these parameters were set as $\varepsilon_\infty = 5.6$, $\omega_\mathrm{p} = 2.1981 \times 10^{13}$ rad s^{-1}, and $\gamma = 5.117 \times 10^{11}$ rad s^{-1}.

QUANTITATION AND STATISTICAL ANALYSIS

The simulation data is produced by COMSOL Multiphysics software. The THz emission signals is measured by a THz emission spectroscopy system. Figures shown in the main text were produced by ORIGIN from the raw data.

ADDITIONAL RESOURCES

Any additional information about the simulation and data reported in this paper is available from the lead contact on request.